Electron Vortex Beams with High Quanta of Orbital Angular Momentum

Benjamin J. McMorran,[1]* Amit Agrawal,[1,2] Ian M. Anderson,[3] Andrew A. Herzing,[3] Henri J. Lezec,[1] Jabez J. McClelland,[1] John Unguris[1]

Electron beams with helical wavefronts carrying orbital angular momentum are expected to provide new capabilities for electron microscopy and other applications. We used nanofabricated diffraction holograms in an electron microscope to produce multiple electron vortex beams with well-defined topological charge. Beams carrying quantized amounts of orbital angular momentum (up to $100\hbar$) per electron were observed. We describe how the electrons can exhibit such orbital motion in free space in the absence of any confining potential or external field, and discuss how these beams can be applied to improved electron microscopy of magnetic and biological specimens.

The discovery that optical vortices—light beams with a spiral phase singularity at the center of helical wavefronts—carry orbital angular momentum (OAM) (1) has led to appreciable advances in optical microscopy (2, 3), astronomy (4), micromanipulation (5), quantum state manipulation (6, 7), and other diverse applications (8). In an effort to extend these applications to other types of beams, we demonstrate the production of well-separated electron vortex beams with large quantized angular momentum. Electron vortices provide novel opportunities in electron microscopy.

An optical vortex beam can be characterized by the topological charge, m, describing the magnitude of the phase singularity at the center of the vortex. The wave functions of all such optical vortices include a phase winding factor, $\exp(im\varphi)$, where φ is the azimuthal angle about the optical axis z. This phase factor can be imprinted onto a conventional Gaussian beam, described in cylindrical coordinates as

$$G(\rho,z) \propto$$
$$\frac{1}{w(z)}\exp\left\{-i\left[\frac{2\pi z}{\lambda} + \frac{\pi\rho^2}{\lambda R(z)} - \zeta(z)\right]\right\}$$
$$\times \exp\left[\frac{-\rho^2}{w(z)^2}\right] \qquad (1)$$

where ρ is the radial distance from the optical axis, $w(z)$ is the beam width, $R(z)$ is the radius of wavefront curvature, $\zeta(z)$ is the Guoy phase, and λ is the wavelength. When this imprinting occurs, the result is a particularly simple kind of optical vortex called a Laguerre-Gaussian (LG) beam, described by the wave function

$$\psi_{LG}(\rho,\varphi,z) =$$
$$G(\rho,z)\left[\frac{\sqrt{2}\rho}{w(z)}\right]^{|m|}\exp\left\{i\left[m\varphi + |m|\zeta(z)\right]\right\} \qquad (2)$$

For $m \neq 0$, complete destructive interference at the vortex core yields an intensity node along the entire optical axis of the vortex, such that

LG beams are hollow and form characteristic ring-shaped (annular) intensity distributions when projected on a planar detector. An application of the angular momentum operator $\hat{L}_z = -i\hbar\partial_\varphi$ to this wave function shows that the optical vortex carries a quantized projection of OAM onto the optical axis, such that $L_z = m\hbar$ (where $\hbar$ is Planck's constant divided by 2π). The optical vortex is an orbital eigenstate for the individual particles that make up the beam (6).

Massive particles, such as free electrons, can also occupy such vortex states. The similarity between the Schrödinger equation describing the evolution of free-particle wave functions and the Helmholtz equation describing the propagation of light suggests that matter waves can be manipulated and applied in similar ways to light waves. The fact that LG beams are stable paraxial solutions of both the Helmholtz equation and the Schrödinger equation led to predictions (9, 10) that free electron vortices were not only physically realizable but they could also be produced and applied in analogous ways to optical vortices. The first demonstration of electron vortex beams used a nanoscale spiral phase plate (11), formed by three pieces of thin graphite. However, it is very difficult to generate smooth helical wavefronts
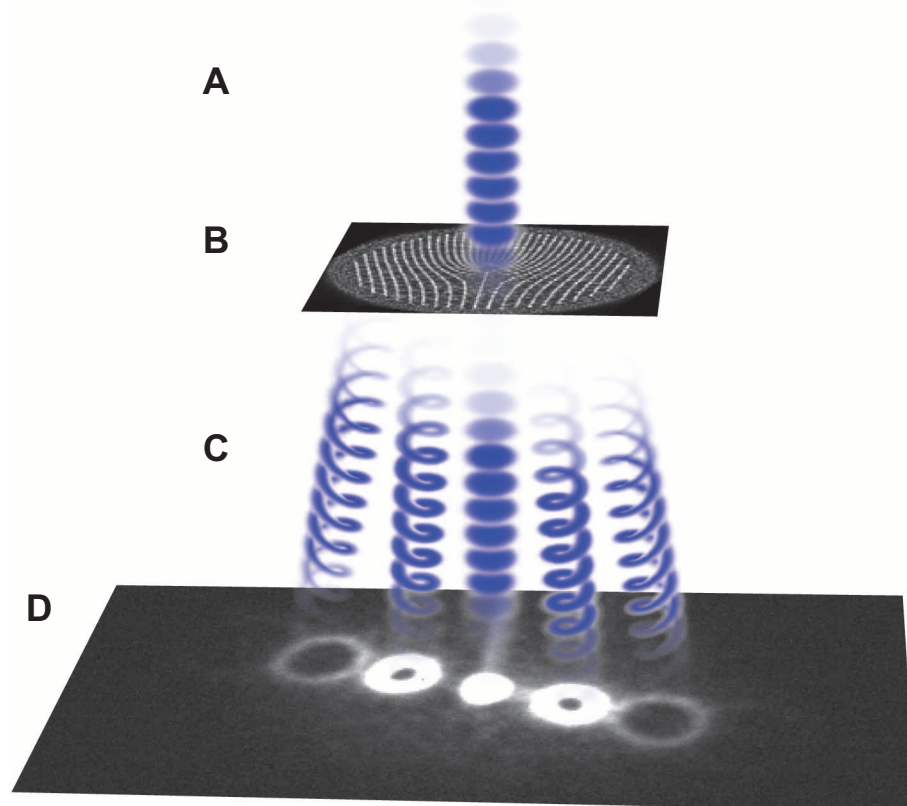

Fig. 1. Representation of the formation of electron vortices. (**A** to **D**) A spatially coherent plane wave of electrons (A) illuminates a nanofabricated hologram (B) and then diffracts into multiple electron vortex beams (C), which are then imaged (D) using a CCD (charge-coupled device). The depictions of the vortex beams shown at (C) simulate the wavefronts of the electrons, not their trajectories. The beam cross section shown in (D) is a measured diffracted electron intensity distribution. For simplicity, the TEM imaging optics used to demagnify the diffraction pattern are not shown here.

[1]Center for Nanoscale Science and Technology, National Institute of Standards and Technology, Gaithersburg, MD 20899, USA. [2]Maryland NanoCenter, University of Maryland, College Park, MD 20742, USA. [3]Surface and Microanalysis Science Division, National Institute of Standards and Technology, Gaithersburg, MD 20899, USA.

*To whom correspondence should be addressed. E-mail: mcmorran@nist.gov

using this approach, and it was noted that the resulting electron vortices had noninteger topological charge, such that the electrons occupied mixed quantized orbital states (*12*). Microscale gratings were recently used to create electron vortex beams with topological charge *m* = 1 (*13*).

We use nanoscale diffraction holograms to produce free electrons with large angular momentum in pure quantized orbital states (Fig. 1). Our work is based on earlier demonstrations using nanofabricated gratings for coherent electron interferometry (*14–16*), which led to a proposal to apply similar techniques to generate electron vortices (*10*). This approach, also adopted by (*13*), uses a grating mask with a fork dislocation to holographically imprint a phase vortex onto a diffracted beam (*17, 18*). Advantages of this technique over spiral phase plates are that the diffracted beam automatically possesses integer topological charge, regardless of the wavelength, and it can be scaled to generate vortices with large quanta of OAM by including a higher-order fork dislocation. Transmission of a beam with wavelength λ through a binary hologram with slit spacing *d* (the grating period) and a fork dislocation defined by *b* additional half-slits produces multiple diffracted vortex beams. The *n*th diffraction order has distinct topological charge $m = nb$, such that negative diffraction orders propagating to one side of the central order beam have quantized OAM that is antiparallel to the propagation direction, and vice versa for positive diffraction orders. The diffracted beams propagate at discrete angles $\alpha = \lambda/d$ relative

to one another, so for applications requiring isolated electron vortex beams it is necessary to use holograms with sufficiently small grating periods.

With a view toward future applications requiring high-quality isolated electron vortex beams, we have placed a particular emphasis on fabricating diffraction holograms with nanoscale feature sizes. Using a focused ion beam to mill silicon nitride membranes (*19*), we made multiple transmission holograms with grating periods of 50, 75, and 100 nm over circular areas 5 μm in diameter, featuring fork dislocations that encode various amounts of topological charge, from $b = 1$ to $b = 25$ (Fig. 2, A and B). These holograms have grating periods that are an order of magnitude smaller than those demonstrated in (*13*); this provides a correspondingly larger separation angle between beams. The smaller feature size also allows higher topological charge to be encoded within the same finite aperture area, enabling us to demonstrate electron beams with OAM up to 100ℏ.

The electron vortices are produced by diffraction from the holograms in a transmission electron microscope (TEM) operating at 300 keV (*19*). Images of the diffraction patterns (Fig. 2 and Fig. 3) show the ring-shaped projections of electron vortex beams onto the detector plane. Electron vortex beams with distinct topological charge are selectively generated in particular diffraction orders from different holograms. In Fig. 3, one can discern the fourth diffraction order produced by a grating with dislocation

number $b = 25$ (Fig. 2B). The corresponding topological charge in this beam is $m = 100$, and it is composed of individual electrons that each carry 100ℏ quanta of OAM. Electrons that have such high OAM are localized to a thin annulus around a large hollow core.

The free-space evolution of a hollow core in a wave function can be used to determine the existence of a vortex. A wave function with OAM has zero amplitude at the vortex core because of the repulsive centrifugal barrier. This is manifested in an LG beam by a central node that persists through the focus and increases in diameter as a function of distance from the beam waist. On the other hand, an initially ring-shaped wave function without OAM, such as that formed with an annular beam-defining aperture, will spread radially both inward and outward, such that the hole at the center of the wave becomes smaller and eventually disappears. We measured the hollow structure of the electron vortex beam by focusing it in space and then imaging the beam at multiple transverse planes relative to the beam waist (Fig. 4A) (*19*). The dark core can be observed throughout the Rayleigh range of each diffracted electron beam. Intensity line profiles through the first diffraction order, an $m = 15$ beam, show that the dark vortex core increases in diameter with distance from the focus (Fig. 4B). A quantitative analysis shows that over this range the vortex core diameter increases away from the beam waist by a factor of 2.8 ± 0.4 (fig. S1), which indicates that the diffracted electron

Fig. 2. Nanofabricated gratings with fork dislocations (top row) used to create electron beams with quantized phase vortices (bottom row). (**A** and **B**) A spatially coherent beam of 300-keV electrons transmitted through (A) a grating with period of 75 nm and *b* = 1, and (B) a grating with period of 100 nm and *b* = 25 (dislocations magnified in insets). The area around the central dislocation in (B) has been masked off to preserve structural integrity. (**C** and **D**) The diffraction patterns formed by (A) and (B), respectively. Each ring-shaped spot in (C) and (D) is the transverse intensity profile of an electron vortex beam. The topological charge is indicated below each diffracted beam. The diffracted electron intensity distributions are shown in false color to make the higher diffraction orders more evident.
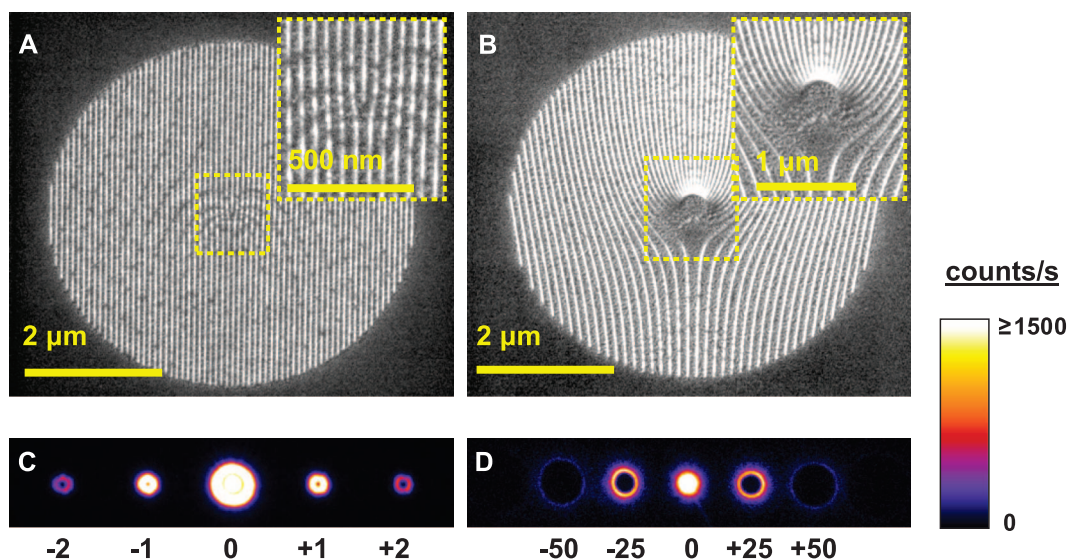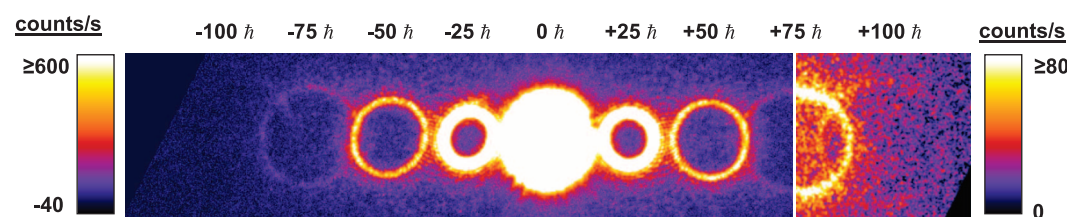

Fig. 3. Electron vortices with large OAM. The false-color image shows transverse intensity profiles of electron vortex beams produced using the hologram shown in Fig. 2C. The labels indicate the associated values of L_z possessed by each electron in an order. An electron vortex with $L_z = +100ℏ$ (*m* = 100) is evident with a different color scale applied to the right side of the image, containing the fourth and part of the third diffraction orders.
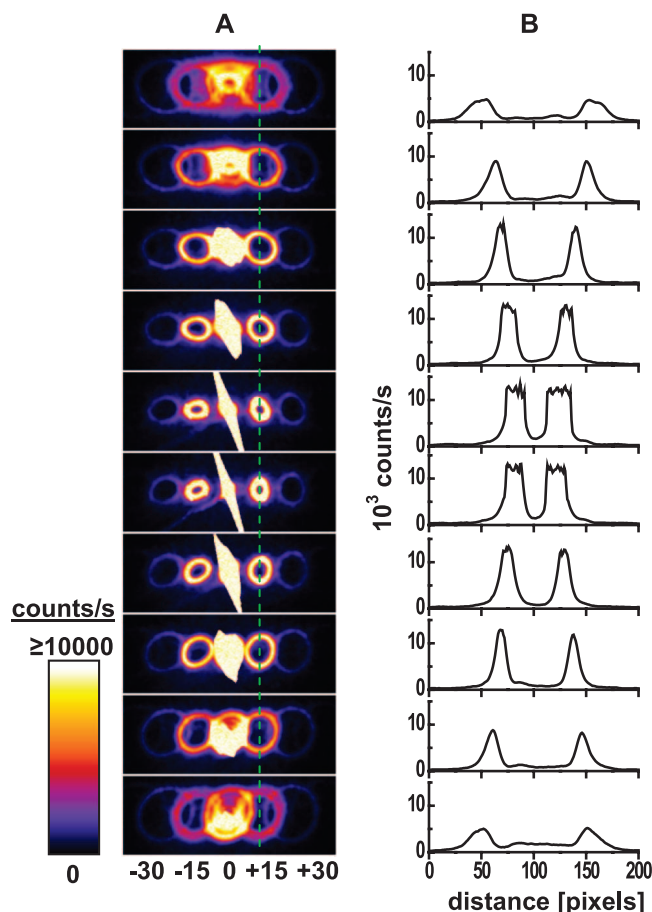
Fig. 4. Evolution of electron vortex beams going through focus. (**A**) A focal series of images shows multiple diffracted electron vortex beams going through a beam waist. The beams are produced using a grating with a dislocation of $b = 15$. The slanted elongation of the intense central beam near the beam waist is an artifact resulting from saturation of the CCD camera. (**B**) Line profiles though the first diffraction order [indicated by the dashed green line in (A)] clearly show the presence of a persistent central intensity node that expands from the beam waist, indicating a phase vortex and therefore OAM. (**C**) A simulation of the wavefronts and transverse amplitude of an $m = 5$ Laguerre-Gaussian beam going through focus illustrates the helical structure of the wavefronts. (**D**) A geometric (ray) optics model reveals that the electron vortex beam can be understood as a superposition of semiclassical straight-line trajectories.

beams possess angular momentum. An interference experiment between the electron vortex beam and a plane wave confirmed that this OAM is due to a helical phase (fig. S2).

These results show that electrons can be prepared in quantized orbital states with large OAM, in free space devoid of any central potential, electromagnetic field (*20*), or medium that confines the orbits. The electron vortex state is nonradiative in free space, as it must be, because emission of a photon would violate the simultaneous conservation of energy and linear momentum. Unlike a classical vortex, this orbital motion cannot be attributed to the collective behavior of many electrons in the beam; at the low beam currents of this experiment, the separation between individual electrons along the optical axis is several orders of magnitude larger than the longitudinal extent of each wave packet (*21*). Such high-OAM electron vortex states can exist at rest, too, because (unlike in a beam of photons) one can produce, using a decelerating electric field, a reference frame in which the forward motion of the electron vortex is zero along the optical axis.

The electron vortex is understandable in terms of semiclassical physics, provided the correct model is used for how these states evolve in time. In the reference frame where the electron vortex has no forward motion, the wave function

is uniformly delocalized in a ring. The radius of this ring-shaped vortex wave function may change with time, but the centroid of the wave function is stationary. Thus, there is no acceleration associated with the electron's center of mass, and so no external force is necessary to preserve or define the orbital motion. A picture of this wave function evolving in space is provided by the simulation of a focused LG beam (Fig. 4C). The helical wavefronts of the beam are slightly tilted both azimuthally and radially, such that their locus of peak amplitude sweeps out a hyperboloid surface that can be described as a family of straight lines (Fig. 4D). Thus, the electron vortex can be modeled simply as a coherent superposition of classical straight trajectories that are slightly skewed and offset from the optical axis of the vortex (*22*).

Electron vortex beams are expected to provide new capabilities for electron energy-loss spectroscopy (EELS) in a TEM (*23*). Computed scattering cross sections between electron vortices and atoms show that it is possible for the electron vortex to transfer both quantized OAM and energy to the atoms. This transfer could be used to induce atomic transitions that were previously inaccessible in conventional EELS, such that an OAM-dependent signal could provide new chemical, crystallographic, optical, electronic,

and magnetic information about a sample. This finding was recently confirmed experimentally (*13*). We are particularly interested in developing this technique for magnetic imaging, which will require the use of well-separated electron vortex beams.

Electron vortices can also enable spiral phase microscopy (*2, 24*) in a TEM, enhancing the visibility of edges in samples with low absorption contrast, such as unstained biological specimens, without sacrificing spatial resolution. Computer-generated holograms have been used to implement spiral phase measurements in transmission light microscopes (*24*). Nanofabricated holograms could be implemented in a similar way in a TEM, provided that the hologram provides sufficient angular separation between vortex beams. This technique could provide some advantages over emerging TEM phase plate technologies (*25, 26*), because the spiral phase provides additional information (*2*). This improved phase contrast will be relevant for TEM imaging of electron-transparent samples, such as biological specimens, macromolecules, carbon nanotubes, and polymers.

References and Notes
1. L. Allen, M. W. Beijersbergen, R. J. C. Spreeuw, J. P. Woerdman, *Phys. Rev. A* **45**, 8185 (1992).
2. S. Fürhapter, A. Jesacher, S. Bernet, M. Ritsch-Marte, *Opt. Lett.* **30**, 1953 (2005).

3. S. W. Hell, *Nat. Biotechnol.* **21**, 1347 (2003).
4. G. Foo, D. M. Palacios, J. Swartzlander Jr., *Opt. Lett.* **30**, 3308 (2005).
5. D. G. Grier, *Nature* **424**, 810 (2003).
6. A. Mair, A. Vaziri, G. Weihs, A. Zeilinger, *Nature* **412**, 313 (2001).
7. M. F. Andersen *et al.*, *Phys. Rev. Lett.* **97**, 170406 (2006).
8. S. Franke-Arnold, L. Allen, M. Padgett, *Laser Photon. Rev.* **2**, 299 (2008).
9. K. Bliokh, Y. Bliokh, S. Savel'ev, F. Nori, *Phys. Rev. Lett.* **99**, 190404 (2007).
10. B. J. McMorran, thesis, University of Arizona (2009).
11. M. Uchida, A. Tonomura, *Nature* **464**, 737 (2010).
12. J. Leach, E. Yao, M. J. Padgett, *N. J. Phys.* **6**, 71 (2004).
13. J. Verbeeck, H. Tian, P. Schattschneider, *Nature* **467**, 301 (2010).
14. B. McMorran, J. D. Perreault, T. A. Savas, A. Cronin, *Ultramicroscopy* **106**, 356 (2006).
15. A. Cronin, B. McMorran, *Phys. Rev. A* **74**, 061602(R) (2006).
16. B. J. McMorran, A. D. Cronin, *N. J. Phys.* **11**, 033021 (2009).
17. V. Y. Bazhenov, M. V. Vasnetsov, M. S. Soskin, *JETP Lett.* **52**, 429 (1990).
18. N. R. Heckenberg, R. McDuff, C. P. Smith, H. Rubinstein-Dunlop, M. J. Wegener, *Opt. Quantum Electron.* **24**, S951 (1992).
19. See supporting material on *Science* Online.
20. Although the beams in this experiment do traverse magnetic fields in the lenses, the fields are confined to very small intervals relative to the entire path of the electrons.
21. Assuming a 1-nA, 300-keV electron beam with 0.3-eV energy spread, the longitudinal extent of a electron's wave packet along the optical axis is about 3 μm, whereas the average separation distance between consecutive electrons is 4 cm.
22. A. V. Volyar, V. G. Shvedov, T. A. Fadeeva, *Tech. Phys. Lett.* **25**, 203 (1999).
23. R. F. Egerton, *Electron Energy-Loss Spectroscopy in the Electron Microscope* (Springer, New York, 1996).
24. A. Jesacher, S. Fürhapter, S. Bernet, M. Ritsch-Marte, *Phys. Rev. Lett.* **94**, 233902 (2005).
25. R. Danev, H. Okawara, N. Usuda, K. Kametani, K. Nagayama, *J. Biol. Phys.* **28**, 627 (2002).
26. K. Schultheiß, F. Pérez-Willard, B. Barton, D. Gerthsen, R. R. Schröder, *Rev. Sci. Instrum.* **77**, 033701 (2006).
27. We thank S. Adam, G. Gallatin, M. Stiles, and J. H. Scott for useful discussions. Supported by the NIST-CNST NanoFab, NIST Division 637 FIB-SEM, and the NIST-CNST/UMD-NanoCenter Cooperative Agreement. The authors declare no competing financial interests.

Solvent-Free Oxidation of Primary Carbon-Hydrogen Bonds in Toluene Using Au-Pd Alloy Nanoparticles

Lokesh Kesavan,[1] Ramchandra Tiruvalam,[2] Mohd Hasbi Ab Rahim,[1] Mohd Izham bin Saiman,[1] Dan I. Enache,[1] Robert L. Jenkins,[1] Nikolaos Dimitratos,[1] Jose A. Lopez-Sanchez,[1] Stuart H. Taylor,[1] David W. Knight,[1] Christopher J. Kiely,[2] Graham J. Hutchings[1]*

Selective oxidation of primary carbon-hydrogen bonds with oxygen is of crucial importance for the sustainable exploitation of available feedstocks. To date, heterogeneous catalysts have either shown low activity and/or selectivity or have required activated oxygen donors. We report here that supported gold-palladium (Au-Pd) nanoparticles on carbon or TiO$_2$ are active for the oxidation of the primary carbon-hydrogen bonds in toluene and related molecules, giving high selectivities to benzyl benzoate under mild solvent-free conditions. Differences between the catalytic activity of the Au-Pd nanoparticles on carbon and TiO$_2$ supports are rationalized in terms of the particle/support wetting behavior and the availability of exposed corner/edge sites.

Selective oxidation of primary carbon-hydrogen bonds is of crucial importance in activating raw materials to form intermediates and final products for use in the chemical, pharmaceutical, and agricultural business sectors (*1*). One class of raw materials is alkyl aromatics; toluene, for example, the simplest member of this class, can be oxidized to benzyl alcohol, benzaldehyde, benzoic acid, and benzyl benzoate. These products are commercially significant as versatile intermediates in the manufacture of pharmaceuticals, dyes, solvents, perfumes, plasticizers, dyestuffs, preservatives, and flame retardants. Commercially, benzaldehyde is produced by the chlorination of toluene followed by saponification (*2*), and benzoic acid is produced by the liquid-phase cobalt-catalyzed reaction of toluene using oxygen at 165°C with acetic acid as solvent, but the conversion has to be limited to <15% to retain high selectivities (*3*–*9*). The use of halogens and acidic solvents makes these pro-

cesses environmentally unfriendly. Vapor-phase oxidation has been considered, but the conversion must be limited to avoid overoxidation to CO$_2$ and other byproducts (*10*). Attempts to overcome these problems have prompted investigation of the use of supercritical CO$_2$ and ionic liquids, but these unfortunately resulted in low conversions (*11*, *12*).

Often, heterogeneous catalysts are preferred over homogeneous catalysts, because these materials can be readily separated from the reaction mixture. Heterogeneous catalysts can also be readily used in flow reactors, facilitating the efficient production of materials using continuous processes. For the oxidation of toluene, there have been many attempts to find a suitable oxidation catalyst, and to date these have used copper and manganese (*13*–*15*), cobalt (*16*), or chromium (*17*) catalysts, but all of these perform very poorly with turnover numbers (TONs: mole of product per mole of metal catalyst) of less than 100, even at temperatures in excess of 190°C (table S1) (*18*). There is clearly a need to develop heterogeneous catalysts for toluene oxidation that have greatly improved activity while retaining selectivity.

Recently, we have shown that Au-Pd alloy nanoparticles are very effective for the direct synthesis of hydrogen peroxide (*19*) and the oxi-

dation of primary alcohols using oxygen (*20*). This catalyst operates by establishing a reactive hydroperoxy intermediate. Because these intermediates are known to be involved in the enzymatic oxidation of primary carbon-hydrogen bonds (*21*), we reasoned that it should be feasible for Au-Pd nanoparticles to be active for the oxidation of the primary carbon-hydrogen bonds in toluene. Here we show that Au-Pd alloy nanoparticles prepared by a sol immobilization technique can give significantly improved activity for the oxidation of toluene under mild solvent-free conditions. These catalysts have TONs that are a factor of ~30 greater than those of previous heterogeneous catalysts for this reaction and also display a remarkably high selectivity to benzyl benzoate.

We started by investigating the oxidation of toluene in an autoclave reactor with O$_2$ in the absence of catalyst in order to determine the blank baseline rate. O$_2$ is a di-radical and can initiate homogeneous oxidation processes at elevated temperatures and pressures. We found that such processes become substantial at 190°C under our conditions (fig. S1) (*18*). This important observation suggests that the earlier studies conducted at 190°C (table S1) (*18*) may not in fact have been heterogeneously catalyzed. In view of the potential role of O$_2$ di-radicals, the maximum reaction temperature in our studies has been restricted to 160°C; at this temperature, the blank reaction in the absence of catalyst but in the presence of support is negligible for short reaction times (Table 1, entries 1, 3, and 4) and is very low at longer reaction times (Table 1, entry 2). We initially investigated Au-Pd/TiO$_2$ catalysts, prepared by impregnation, because these had previously been shown to be very active for H$_2$O$_2$ synthesis (*19*) and alcohol oxidation (*20*); however, these catalysts were not found to be particularly active for toluene oxidation, although they did not produce any CO$_2$ (table S2) (*18*).

The Au-Pd nanoparticles synthesized by the impregnation method can be relatively large (typically >6 nm) and have substantial compositional variations, which limits their reactivity. Therefore, in order to design more effective catalysts, we decided to investigate Au-Pd nanoparticles with smaller median particle sizes (2 to

[1]Cardiff Catalysis Institute, School of Chemistry, Cardiff University, Main Building, Park Place, Cardiff CF10 3AT, UK. [2]Department of Materials Science and Engineering, Lehigh University, 5 East Packer Avenue, Bethlehem, PA 18015–3195, USA.

*To whom correspondence should be addressed. E-mail: hutch@cardiff.ac.uk

Electron Vortex Beams with High Quanta of Orbital Angular Momentum

Benjamin J. McMorran *et al.*
Science **331**, 192 (2011);
DOI: 10.1126/science.1198804